Nanoscale

RSC Publishing

PAPER

View Article Online
View Journal | View Issue

Facile and effective synthesis of hierarchical TiO_2 spheres for efficient dye-sensitized solar cells†

Cite this: *Nanoscale*, 2013, **5**, 6577

Meidan Ye, Chang Chen, Miaoqiang Lv, Dajiang Zheng, Wenxi Guo and Changjian Lin*

Three-dimensional (3D) crystalline anatase TiO_2 hierarchical spheres were successfully derived from Ti foils *via* a fast, template-free, low-temperature hydrothermal route followed by a calcination post-treatment. These dandelion-like TiO_2 spheres are composed of numerous ultrathin nanoribbons, which were subsequently split into fragile nanoflakes as a result of the decomposition of Ti-complex intermediates to TiO_2 and H_2O at high temperature. The dye-sensitized solar cells (DSSCs) employing such hierarchically structured TiO_2 spheres as the photoanodes exhibited a light-to-electricity conversion efficiency of 8.50%, yielding a 28% enhancement in comparison with that (6.64%) of P25-based DSSCs, which mainly benefited from the enhanced capacity of dye loading in combination with effective light scattering and trapping from hierarchical architecture.

Received 1st April 2013
Accepted 10th May 2013

DOI: 10.1039/c3nr01604h

www.rsc.org/nanoscale

1 Introduction

Semiconductor nanostructures are presently a focal research issue because of their electrochemical, photochemical and biological properties and their potential applications in solar cells,[1,2] photocatalysis,[3] hydrogen generation,[4,5] Li-ion batteries,[6] sensors,[7] *etc.* In recent years, great effort has been devoted to the design and synthesis of semiconductor nanocrystals with controlled shape, size and crystal structure on account of the strong influence on their properties and functions, consequently, on the performances in many hi-tech applications.[3,8–11]

As one of the most important semiconductors with a wide band gap, TiO_2 has been extensively studied and applied in a great many fields due to its excellent physical and chemical properties.[12,13] In particular, nanostructured TiO_2 materials have already attracted considerable attention in virtue of their superior performance to traditional bulk structured materials.[13] To date, varieties of TiO_2 morphologies, including nanoparticle,[14] nanotube,[15,16] nanowire,[17] nanosheet,[18] three-dimensional (3D) architecture[19] and mesoporous nanostructure,[20] have been successfully realized through various approaches (*e.g.*, sol–gel synthesis,[21] electrochemical anodization,[22,23] electrospray[24] and hydrothermal[20] or solvothermal[25] processing). Among these, the organization of complex micro- and nano-structures, especially 3D hierarchical architectures by assembling nanoscale building blocks such as nanosheets,[26] nanoparticles,[20] nanorods,[27] has currently been widely investigated. The hierarchical TiO_2 structure takes advantage of the properties of nanometer-sized building blocks as well as micron- or submicron-sized assemblies and then displays attractive properties different from their nanoscaled building blocks, for example, efficient light scattering from microsized 3D structures and better penetration of electrolytes through the relatively large interspaces between 3D structures.[8,28] Thus, developing feasible approaches to construct hierarchically structured TiO_2 materials with adjustable optical, electronic, and catalytic responses significantly makes a contribution to the field of nanoscale science. So far, several synthetic strategies, for example, template-assisted synthesis,[29,30] induced self-assembly growth[1,3] and electrochemical processes,[6,24] have been employed for the fabrication of versatile hierarchical TiO_2 morphologies.

However, in many cases, the synthesis procedures are carried out under special conditions, such as, template-assistance, high temperature and long duration.[29] For instance, since the pioneering work on nanotubular titanate obtained by the hydrothermal treatment of titania with alkaline solution in 1998,[31] various nanostructures, such as nanotubes,[6,32] nanowires,[33] and nanosheets,[34,35] have been widely developed due to their unique structures and attractive potential applications. In particular, assembly of titanate or its derived TiO_2 nanostructures into hierarchical morphologies has currently caught much interest.[1,6,26,29,36] However, many synthesis processes are performed by using organics as chelating agents,[3] at high temperature,[1,33] long growth time[6,26] or high NaOH concentration.[36] Thus, it is still a great challenge to develop facile and effective methods for fabrication of well-defined 3D TiO_2

State Key Laboratory of Physical Chemistry of Solid Surfaces, Department of Chemistry, College of Chemistry and Chemical Engineering, Xiamen University, Xiamen 361005, China. E-mail: cjlin@xmu.edu.cn

† Electronic supplementary information (ESI) available: FESEM images of samples prepared in other control experiments and a cross-sectional view of the three films. See DOI: 10.1039/c3nr01604h

hierarchical structures with excellent properties, such as large surface area and great light scattering ability.

In this regard, here we report an effective hydrothermal process for the easy synthesis of a 3D TiO_2 superstructure. A dandelion-like sphere assembled by numerous ultrathin nanoribbon building blocks was achieved *via* a low-temperature hydrothermal process with a fast growth rate in a H_2O_2 aqueous solution containing a small amount of NaOH. These titania spheres were subsequently transformed into crystalline TiO_2 spheres *via* a thermal treatment. Further evaluation of the synthesized 3D TiO_2 superstructure as the photoanode in DSSCs showed a remarkable performance in the power conversion efficiency.

2 Experimental section

2.1 Formation of hierarchically structured TiO_2 materials

Hierarchical TiO_2 materials were prepared based on a hydrothermal procedure. In a typical synthesis, some Ti foils were placed in a 50 mL Teflon-lined autoclave which contains 15 mL of DI water, 15 mL of hydrogen peroxide (H_2O_2, 30 wt%) and 0.3 M NaOH, and then heated at 80 °C for 1 h. The autoclave was then cooled to room temperature in air. The obtained precipitates were filtered, washed several times using distilled water and then 0.1 M HCl solution, dried in an oven at 60 °C for 2 h, annealed at 450 °C for 2 h, and finally collected for further characterization. In control experiments, hydrothermal conditions were changed, including temperature (*e.g.*, 60 °C, 100 °C), NaOH concentration (*e.g.*, 3 M) and H_2O_2 volume (*e.g.*, 1.5 mL).

2.2 TiO_2 solar cell fabrication

The hierarchical TiO_2 structure paste was prepared by mixing 0.3 g of the as-obtained TiO_2 sphere powder and 0.5 g of polyethylene glycol (PEG, mole weight = 20 000) in 1 mL of DI water and 1 mL of ethanol.[37] It was then deposited by the doctor blade method on a clean fluorine-doped tin oxide (FTO) glass which was ultrasonically cleaned for 30 min in a mixed solution of acetone and ethanol with a volume ratio of 1 : 1, followed by rinsing with deionized water for 15 min. After a heating process at 450 °C for 30 min to remove the organic substances, the TiO_2 films were soaked in 0.2 M $TiCl_4$ aqueous solution at 70 °C for 40 min followed by another annealing treatment at 450 °C for 30 min. For comparison, P25 TiO_2 films and a bi-layered film (*i.e.*, a hierarchical TiO_2 sphere scattering cover layer deposited on a P25 TiO_2 main-layer) were also prepared *via* the same process. To fabricate DSSCs, all TiO_2 films described above were soaked in anhydrous ethanol containing 0.3 mM commercially available N719 dye (*cis*-diisothiocyanato-bis(2,2′-bipyridyl-4,4′-dicarboxylato) ruthenium(II) bis(tetrabutylammonium); Solaronix Co.) for 24 h at room temperature. Platinum (Pt) counter electrodes were prepared by dropping 0.5 mM H_2PtCl_6 isopropanol solution on the FTO glass, followed by heating at 400 °C for 20 min. Dye-sensitized TiO_2 films with an active area of approximately 0.15 cm^2 were assembled together with the Pt-coated FTO glass by applying a 25 μm thick hot-melt sealed film as the spacer (SX1170-25; Solaronix Co.). The liquid electrolyte used here was acetonitrile solution containing the I_3^-/I^- redox couple (60–70 wt% acetonitrile, 20–25 wt% 1,2-dimethyl-3-propylimidazolium iodide, 1–4 wt% LiI, 5–10 wt% *tert*-butylpyridine and 1–4 wt% I_2), which is commercially available (CJX-EH, CasJuxin Solar Technology Co., Ltd., China). The electrolyte was injected between two electrodes and driven by capillary force through the hole on the hot-melt sealed film.[38]

2.3 Characterization

The morphology and microstructure of nanospheres were examined by field emission scanning electron microscopy (FESEM, HITACHI S-4800) and transmission electron microscopy (TEM, JEOL JEM-2100) with an accelerating voltage of 200 kV. Phase identification of materials was conducted by X-ray diffraction (XRD, PANalytical X'pert PRO). Raman spectrum was recorded on a Renishaw Raman microspectrometer system 2000 equipped with a He–Ne laser (632.8 nm). The N_2 sorption measurements were performed using a Tristar 3000 surface area analyzer (Micromeritics Instrument Corporation). The light absorption of the films was measured by UV-visible spectroscopy (Varian; UV-vis-NIR spectrophotometer, Cary 5000). The performance of the as-prepared DSSCs was evaluated by measuring photocurrent density–photovoltage (*J–V*) curves under AM 1.5G simulated solar light (Oriel 300 W Xe lamp and Newport AM-1.5G filter). The incident-photon-to-current efficiency (IPCE) spectra as a function of wavelength (λ = 400 to 800 nm) were measured using a monochromator (Oriel, Model: 74125). Electrochemical impedance spectra (EIS) were measured on an electrochemical workstation (Autolab, PGSTAT30, Metrohm) equipped with an Autolab LED driver kit. EIS measurements were carried out under illumination and open circuit conditions with a 627 nm LED light and the frequency range was set from 0.1 to 10^5 Hz. The EIS spectra were fitted by ZSimpWin software using an equivalent circuit.

3 Results and discussion

In the typical hydrothermal condition, a large quantity of products in light yellow can be obtained, which finally became white after the calcination process. Their morphologies were firstly observed using electron microscopes. Fig. 1a and b show the typical SEM images of the as-obtained sample without calcination, exhibiting a spherical morphology consisting of numerous interconnected nanoribbons with a diameter of around 500 nm. After calcination treatment of the spheres at 450 °C for 2 h, it is clearly observed that although the spheres still keep the spherical structure, their building blocks, interconnected nanoribbons, are split into pieces in the form of small and particulate nanoflakes (Fig. 1c), mainly because of the decomposition of Ti-complex intermediates to TiO_2 and H_2O at high temperature.[28] These rough spheres were subsequently prepared into slurry for the preparation of a film as shown in Fig. 1d. Moreover, a mesoporous structure was developed on the as-used Ti foil along with the production of 3D hierarchical spheres (Fig. S1a, ESI†).

Further information about the hierarchical spheres was obtained from TEM and is shown in Fig. 2. Fig. 2a and b exhibit

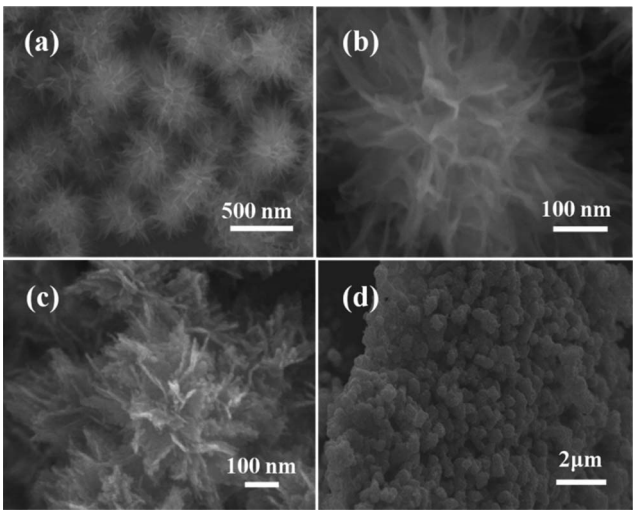

Fig. 1 SEM images of TiO_2 spheres prepared by hydrothermal processing in aqueous solution containing 15 mL of H_2O_2 (30 wt%), 15 mL of DI water and 0.3 M NaOH, with Ti foils as the Ti source at 80 °C for 1 h. (a and b) Without calcination: (a) top view of several spheres; (b) top view of a sphere. (c and d) With calcination at 450 °C for 2 h: (c) top view of several spheres; (d) cross-sectional view of the corresponding film prepared *via* the doctor blade method.

morphologies of the as-obtained spheres before and after calcination treatment, respectively. The results agree well with the observation in SEM images, that is, the sizes of spheres are about 500 nm and still remain constant after calcination treatment, but the building units of spheres have changed from smooth nanoribbons to rough irregular nanoflakes. Furthermore, the HRTEM image (Fig. 2c) reveals that the calcined hierarchical TiO_2 spheres are composed of crystalline anatase TiO_2 nanocrystals with fringe spacing being approximately 0.35 nm corresponding to the (101) plane of the anatase phase. Meanwhile, the SAED pattern (Fig. 2d) also confirms the polycrystalline spheres, and the most distinct three concentric diffraction rings can be assigned to (101), (004) and (200) planes of the anatase TiO_2 from the centre.[3]

In addition, XRD measurements (Fig. 3a) indicate that the as-prepared product can be identical to $H_2Ti_2O_5 \cdot H_2O$ (JCPDS, 47-0124) with diffraction peaks being observed at $2\theta = 24.3°$,

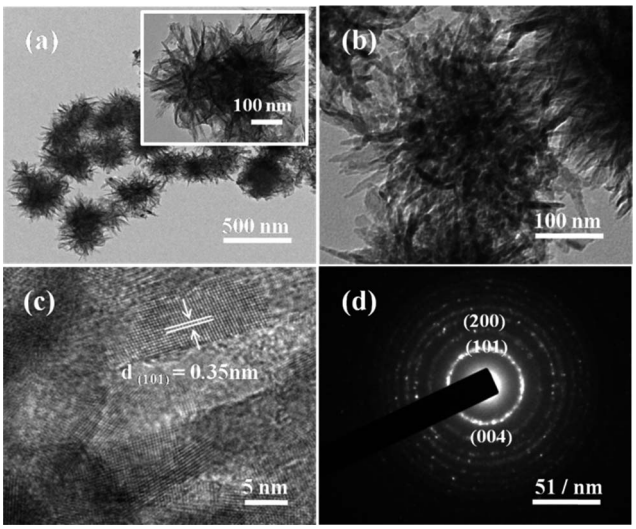

Fig. 2 TEM images of TiO_2 nanospheres: (a) without calcination, (b) with calcination. (c) HRTEM image and (d) electron diffraction pattern of the nanosphere with calcination.

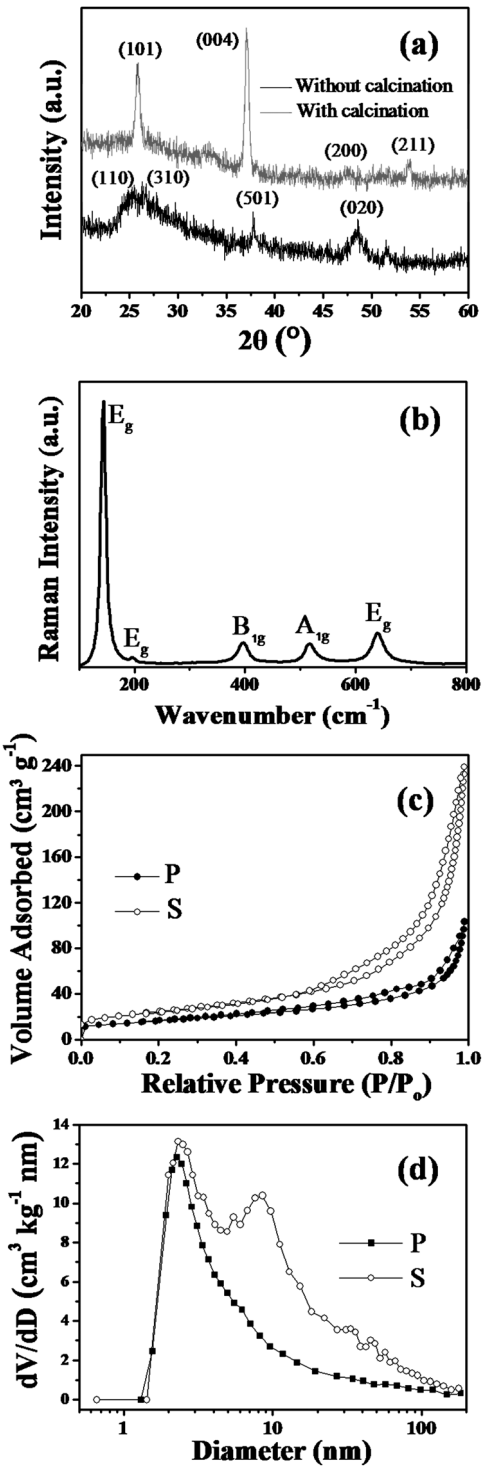

Fig. 3 (a) XRD patterns of TiO_2 spheres without and with calcination, (b) Raman spectra of the as-annealed TiO_2 spheres, (c) N_2 adsorption–desorption isotherms of P25 (denoted as "P") powder and the as-annealed TiO_2 sphere (denoted as "S") powder, and (d) the corresponding pore size distribution plots.

26.8°, 37.6° and 48.5°, corresponding well to those of lattice planes (110), (310), (501) and (020) of the orthorhombic phase.[39] Subsequently, the calcination treatment converted the titanate material into anatase TiO_2, correlating well with the TEM analysis. Moreover, Fig. 3b shows Raman spectra of the annealed TiO_2 spheres, exhibiting an evident identification of the anatase phase from the characteristic Raman modes at 143.8 cm^{-1} (E_g), 196.3 cm^{-1} (E_g), 398.4 cm^{-1} (B_{1g}), 515.8 cm^{-1} (A_{1g}), and 639.4 cm^{-1} (E_g), assigned to the Raman active modes (A_{1g} + B_{1g} + $3E_g$) of anatase, respectively, which is as well in agreement with the analysis from TEM and XRD measurements.[40]

Importantly, the mesoporous nature of hierarchical TiO_2 spheres can be analyzed with N_2 adsorption–desorption isotherm measurements while the corresponding pore size distribution can be determined by using the Barrett–Joyner–Halenda (BJH) method from the desorption branch of the isotherm. As observed in Fig. 5c, the isotherm is typical type IV-like with a type H3 hysteresis loop according to the IUPAC classification, implying the existence of mesopores.[41] The two hysteresis loops in the isotherm suggest that there are both small and large mesopores, which can be verified by the pore size distribution plot in Fig. 3d. The pore size distribution ranges between 2 and 100 nm and the average pore diameter is 16.9 nm. Due to the calcination treatment, the building blocks composed of spheres were converted from smooth nanoribbons to small nanoflakes. Therefore, the BJH analysis of desorption isotherms showed small mesopores with diameters about 2 nm related to interaggregated nanoflakes and large mesopores with diameter about 10 nm associated with the cavities of TiO_2 spheres.[42] Furthermore, the BET surface area of spheres is 104.5 $m^2\ g^{-1}$ and the corresponding volume of pores has a high number of 0.38 $cm^3\ g^{-1}$. Such porosity must be created by the dehydration process during phase transformation. As reference, the average pore diameter, BET surface area and volume of pores for P25 TiO_2 (Fig. 2c and d) are also obtained as 10.9 nm, 58.4 $m^2\ g^{-1}$ and 0.16 $cm^3\ g^{-1}$, respectively. Therefore, it is suggested that the larger surface area and volume of pores for hierarchical TiO_2 spheres by comparison with P25 TiO_2 will contribute to a higher dye uptake and better penetration of electrolyte for the TiO_2 sphere-based DSSCs, consequently, improving the charge harvesting efficiency of devices.

In addition, some control experiments were performed to understand the growth process of the hierarchical TiO_2 spheres. For the temperature parameter, it is demonstrated that lower temperature (*i.e.*, 60 °C) with slower growth rate resulted in larger spheres (*i.e.*, diameter ≈ 700 nm, Fig. S1b, ESI†) while higher temperature (*i.e.*, 100 °C) with faster growth rate led to smaller ones (*i.e.*, diameter ≈ 300 nm, Fig. S1c, ESI†). When reducing the amount of H_2O_2 and increasing the concentration of NaOH, there was no yellow precipitate obtained but only some large fragments were created on the Ti foil (Fig. S1d, ESI†). Similarly, no precipitate was collected in the absence of NaOH (Fig. S1e, ESI†) or H_2O_2 (Fig. S1e, ESI†) in the reaction solution. Basically, the corresponding reaction occurred in the growth process can be described as follows:[36]

$$H_2O_2 + NaOH \rightarrow Na_2O_2 + H_2O \quad (1)$$

$$Na_2O_2 + H_2O \rightarrow NaOH + O_2\uparrow \quad (2)$$

$$H_2O_2 + Ti \rightarrow H_2O + TiO_x \quad (3)$$

$$TiO_x + NaOH \rightarrow Na_2TiO_3 + H_2O \quad (4)$$

$$Na_2TiO_3 + HCl \rightarrow H_2Ti_2O_5\cdot H_2O + NaCl \quad (5)$$

$$H_2Ti_2O_5\cdot H_2O \rightarrow TiO_2 + H_2O\ (\text{calcination}) \quad (6)$$

In brief, the fast formation of plentiful TiO_2 spheres depends on the presence of a large quantity of H_2O_2 for the efficient oxidation of Ti foil to TiO_x, which is subsequently reacted with NaOH to form Na_2TiO_3, followed by an ion exchange with dilute HCl solution to yield $H_2Ti_2O_5\cdot H_2O$, which is finally converted into TiO_2 *via* calcination treatment.

As shown in Fig. S2 (ESI†), a hierarchical TiO_2 sphere film (S, thickness ≈ 20 μm) and a P25 TiO_2 nanoparticle film (P, thickness ≈ 20 μm) as well as a bi-layered film (PS) composed of a hierarchical TiO_2 sphere scattering cover layer (thickness ≈ 10 μm) deposited on a P25 TiO_2 main-layer (thickness ≈ 10 μm) were further exploited as photoanodes to assemble dye-sensitized solar cells (DSSCs), and their performances were recorded (see Experimental methods). Accordingly, the device performances of the above-mentioned N719 dye-sensitized TiO_2-based solar cells are summarized in Table 1 while their corresponding current–voltage (*J–V*) characteristics are shown in Fig. 4a.

Significantly, a markedly enhanced device performance was obtained *via* using the hierarchical sphere photoanodes, exhibiting an improved efficiency (η) of 8.50% achieved for the S-based DSSC in comparison with 6.64% for the P-DSSC. Detailedly, the short-circuit current density (J_{sc}) remarkably increased from 13.54 mA cm^{-2} for the P-based DSSC to 17.88 mA cm^{-2} for the S-based DSSC, which is probably attributed to a larger surface area of the sphere photoanode to uptake more dye molecules. Correspondingly, the adsorbed dye amount (estimated by measuring the eluted dye molecules from films with UV-vis absorption spectroscopy) of the sphere photoanode (116.35 nmol cm^{-2}) is obviously higher than that of the P25 photoanode (94.09 nmol cm^{-2}), which can reasonably support the improved J_{sc} of the S-based DSSC. However, the open circuit voltage (V_{oc}) is 0.73 V and 0.77 V for S-based and P-based DSSCs, respectively. Finally, the S-based DSSC gives a slightly higher fill factor value (0.65 for the S-based DSSC *vs.* 0.64 for the P-based DSSC). In addition, an improved η of 7.85% was also achieved

Table 1 Photovoltaic performance parameters of P-based, S-based and PS-based DSSCs measured under AM 1.5 full sunlight illumination (100 mW cm^{-2})

Sample	J_{sc} (mA cm^{-2})	V_{oc} (V)	FF	η (%)	$N719_{ads}$ (nmol cm^{-2})
P	13.54	0.77	0.64	6.64	94.09
S	17.88	0.73	0.65	8.50	116.35
PS	16.14	0.74	0.66	7.85	104.61

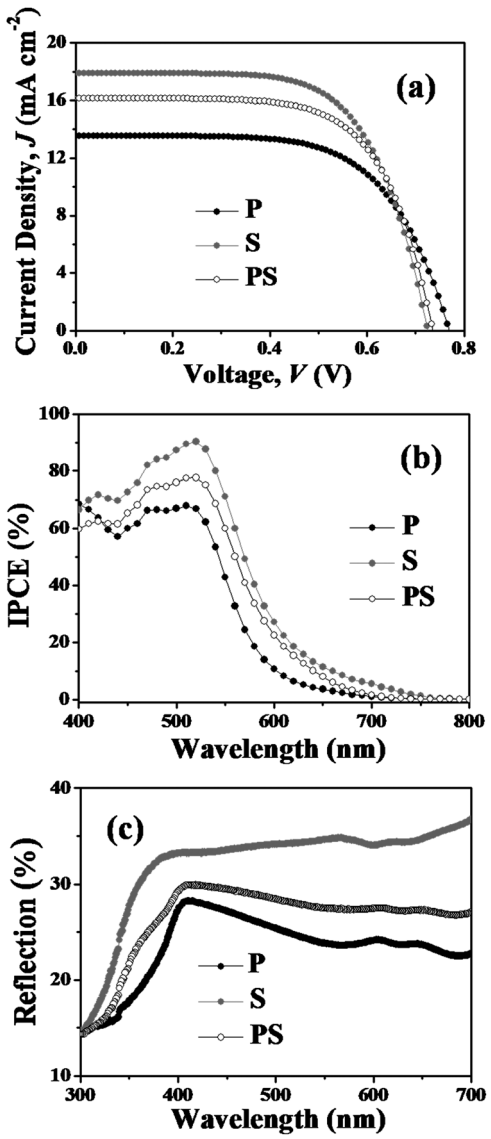

Fig. 4 (a) Current–voltage (*J–V*) characteristics and (b) incident photon to current conversion efficiency (IPCE) curves of P-based (20 μm P25 nanoparticle film), S-based (20 μm sphere film) and PS-based (10 μm nanoparticle + 10 μm sphere film) DSSCs. (c) Diffuse reflectance spectra of the three photoanodes without dye adsorption and electrolyte injection.

for the PS-based DSSC in comparison with that of the P-based DSSC due to the participation of a hierarchical sphere layer (Table 1 and Fig. 4a).

To scrutinize the different photovoltaic performance of these three solar cells, the incident photon-to-current efficiency (IPCE) spectra as a function of wavelength were measured and are exhibited in Fig. 4b. Compared to the P-based DSSC (68%), the IPCE spectrum of the S-based DSSC displays a maximum value of 91% at approximately 520 nm. Furthermore, the IPCE over the entire wavelength region (400–800 nm) of the S-based DSSC was higher than that of the P-based DSSC, implying that the S-based DSSC generated more photoelectrons because of greater dye loading, which was correlated well with the aforementioned dye-loading measurement. Moreover, it is worth noting that the IPCE spectrum of the S-based DSSC reveals an obvious red shift to a longer wavelength (600–750 nm) in comparison with the P-based DSSC due to better light-scattering ability of hierarchical spheres. The light scattering ability of samples was examined by measuring UV-vis diffuse reflectance spectra of the three films with a similar thickness of about 20 μm without dye adsorption. It is indicated that the reflectance over the entire wavelength region (300–700 nm) of the hierarchical sphere film is much higher than that of the P25 nanoparticle film (Fig. 4c). Accordingly, such a hierarchical TiO_2 sphere photoanode would improve the absorption of solar light, then yielding an enhancement in the light harvesting efficiency and, consequently, in J_{sc} (Table 1 and Fig. 4a). As expected, the bi-layered film as well exhibits a larger amount of dye loading (104.61 nmol cm^{-2}), superior light scattering ability (Fig. 4c) and a higher IPCE value (Fig. 4b), which together produce an enhanced J_{sc} (16.14 mA cm^{-2}) and finally an improved η (7.85%) for the PS-based DSSC, as compared to the P-based DSSC (Fig. 4a and Table 1).

In order to better understand the kinetics of electrochemical and photoelectrochemical processes occurring in DSSCs, the analysis of electrochemical impedance spectroscopy (EIS) of the DSSCs noted above was performed under illumination and open-circuit voltage. Fig. 5 demonstrates that the Nyquist plots have two semicircles with a contact series resistance (R_s) on the FTO substrate. The first semicircle in the high frequency range represents the resistance at the counter electrode (R_{pt}) for the

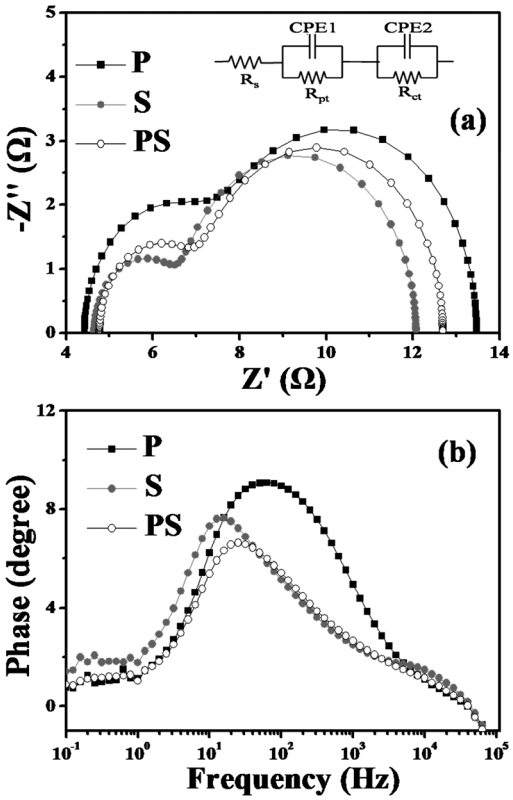

Fig. 5 Nyquist plots (a) and the Bode plots (b) of the DSSCs based on the three types of photoelectrodes.

Table 2 EIS parameters of the three DSSCs obtained by fitting the experimental data according to the equivalent circuit model (inset in Fig. 5a)

Sample	R_s (Ω)	R_{pt} (Ω)	R_{ct} (Ω)	C_μ (F cm^{-2})	τ_r (ms)
P	4.42	3.12	5.93	0.00128	3.18
S	4.65	1.98	5.44	0.00253	10.05
PS	4.77	2.32	5.61	0.00148	6.33

reduction reaction of I_3^- ions in the electrolyte using Pt as the counter electrode. The second semicircle in the intermediate frequency range reflects the charge-transfer resistance (R_{ct}) at interfaces of electrolyte and TiO_2, while the corresponding chemical capacitance (C_μ) describes the density of states in the bandgap of TiO_2.[43] These parameters were achieved by fitting using an equivalent circuit as shown in Table 2 and Fig. 5a. It is found that the R_{ct} value of the S-based DSSC (5.44 Ω) is slightly smaller than that of the P-based DSSC (5.93 Ω), implying a relatively faster electron transfer process at the TiO_2 sphere photoanode interface.[44] Meanwhile, the higher C_μ value of the S-based DSSC indicates that more states on the TiO_2 surface are able to accept electrons from the excited state of the dye, yielding an increased photocurrent. However, this results in a decrease of the photovoltage.[43] In addition, the S-based photoanode also gives a smaller R_{pt} value, which may be associated with the increased concentration of I_3^- in the electrolyte of the S-based DSSC. As mentioned above, the TiO_2 sphere photoanode enhances the light harvesting to photoexcite N719 dye, thus, more I^- should be oxidized to I_3^- to regenerate the dye molecules. It is found that the R_{pt} value is proportional to the square root of the I_3^- concentration within the electrolyte, suggesting that the larger the concentration of I_3^- in the electrolyte, the smaller the counter electrode resistance R_{pt} value.[45] Furthermore, as shown in Fig. 5b, the Bode phase plots of EIS spectra indicate the frequency peaks of the charge transfer process at different interfaces for the three DSSCs. The electron lifetime (τ_r) in DSSCs can be evaluated by the equation of $\tau_r = 1/2\pi f_{max}$, where the characteristic frequency (f_{max}) is the maximum phase shift in the mid frequency peak. Then, it is seen that the S-based DSSC shows higher electron lifetime than those of the other two cells and thus has enhanced power conversion efficiency.[44]

4 Conclusion

In summary, a facile hydrothermal process was developed to prepare 3D hierarchical TiO_2 spheres composed of many ultrathin nanoribbons, which were further transformed into crystalline anatase spheres assembled by nanoflake-shaped petals *via* thermal post-treatment. The DSSC employing such a hierarchical structure as the photoanode showed considerable improvements in photocurrent density (from 13.54 to 17.88 mA cm^{-2}) and power conversion efficiency (from 6.64 to 8.50%) compared to the DSSC using the P25 nanoparticle photoanode, which is mainly attributed to a larger surface area (104.5 m^2 g^{-1} for spheres *vs.* 58.4 m^2 g^{-1} for P25 nanoparticles), enhanced light scattering ability of the hierarchical structure and longer electron lifetime. More importantly, by this facile synthesis method it is feasible to prepare a well-defined hierarchical TiO_2 structure directly derived from Ti foils in large quantity and large scale at low temperature, which is highly beneficial for practical applications.

Acknowledgements

The authors gratefully acknowledge the financial support from the National Natural Science Foundation of China (51072170, 21021002), and the National Basic Research Program of China (2012CB932900).

Notes and references

1 F. Shao, J. Sun, L. Gao, S. W. Yang and J. Q. Luo, *ACS Appl. Mater. Interfaces*, 2011, **3**, 2148–2153.
2 X. Xin, M. He, W. Han, J. Jung and Z. Lin, *Angew. Chem., Int. Ed.*, 2011, **50**, 11739–11742.
3 T. Zhu, J. Li and Q. Wu, *ACS Appl. Mater. Interfaces*, 2011, **3**, 3448–3453.
4 Y. Qiu, K. Yan, H. Deng and S. Yang, *Nano Lett.*, 2011, **12**, 407–413.
5 M. D. Ye, J. J. Gong, Y. K. Lai, C. J. Lin and Z. Q. Lin, *J. Am. Chem. Soc.*, 2012, **134**, 15720–15723.
6 Y. Tang, P. Wee, Y. Lai, X. Wang, D. Gong, P. D. Kanhere, T. T. Lim, Z. Dong and Z. Chen, *J. Phys. Chem. C*, 2012, **116**, 2772–2780.
7 Q. H. Mu, Y. G. Li, H. Z. Wang and Q. H. Zhang, *CrystEngComm*, 2011, **13**, 6258–6264.
8 G. Tian, Y. Chen, W. Zhou, K. Pan, C. Tian, X.-r. Huang and H. Fu, *CrystEngComm*, 2011, **13**, 2994–3000.
9 T. P. Chou, Q. F. Zhang, B. Russo, G. E. Fryxell and G. Z. Cao, *J. Phys. Chem. C*, 2007, **111**, 6296–6302.
10 M. D. Ye, H. Y. Liu, C. J. Lin and Z. Q. Lin, *Small*, 2013, **9**, 312–321.
11 M. Ye, D. Zheng, M. Lv, C. Chen, C. Lin and Z. Lin, *Adv. Mater.*, 2013, DOI: 10.1002/adma.201205274.
12 Y. H. Jang, X. Xin, M. Byun, Y. J. Jang, Z. Lin and D. H. Kim, *Nano Lett.*, 2011, **12**, 479–485.
13 X. Chen and S. S. Mao, *Chem. Rev.*, 2007, **107**, 2891–2959.
14 X. Xin, M. Scheiner, M. Ye and Z. Lin, *Langmuir*, 2011, **27**, 14594–14598.
15 J. Wang and Z. Q. Lin, *Chem. Mater.*, 2008, **20**, 1257–1261.
16 J. Wang, L. Zhao, V. S. Y. Lin and Z. Q. Lin, *J. Mater. Chem.*, 2009, **19**, 3682–3687.
17 J. Y. Chun and J. W. Lee, *Eur. J. Inorg. Chem.*, 2010, **27**, 4251–4263.
18 J. G. Yu, J. J. Fan and K. L. Lv, *Nanoscale*, 2010, **2**, 2144–2149.
19 D. H. Chen, F. Z. Huang, Y. B. Cheng and R. A. Caruso, *Adv. Mater.*, 2009, **21**, 2206.
20 W. Y. Cheng, J. R. Deka, Y. C. Chiang, A. Rogeau and S. Y. Lu, *Chem. Mater.*, 2012, **24**, 3255–3262.
21 B. Koo, J. Park, Y. Kim, S. H. Choi, Y. E. Sung and T. Hyeon, *J. Phys. Chem. B*, 2006, **110**, 24318–24323.
22 J. Wang and Z. Q. Lin, *Chem. Mater.*, 2010, **22**, 579–584.
23 J. Wang and Z. Q. Lin, *J. Phys. Chem. C*, 2009, **113**, 4026–4030.

24 D. Hwang, H. Lee, S.-Y. Jang, S. M. Jo, D. Kim, Y. Seo and D. Y. Kim, *ACS Appl. Mater. Interfaces*, 2011, **3**, 2719–2725.
25 X. J. Lu, F. Q. Huang, X. L. Mou, Y. M. Wang and F. F. Xu, *Adv. Mater.*, 2010, **22**, 3719.
26 N. P. Thuy-Duong, E. J. Kim, S. H. Hahn, W. J. Kim and E. W. Shin, *J. Colloid Interface Sci.*, 2011, **356**, 138–144.
27 J. Zhou, G. Zhao, B. Song and G. Han, *CrystEngComm*, 2011, **13**, 2294–2302.
28 J.-Y. Liao, B.-X. Lei, D.-B. Kuang and C.-Y. Su, *Energy Environ. Sci.*, 2011, **4**, 4079–4085.
29 J. Huang, Z. Huang, W. Guo, M. Wang, Y. Cao and M. Hong, *Cryst. Growth Des.*, 2008, **8**, 2444–2446.
30 S. H. Han, S. Lee, H. Shin and H. Suk Jung, *Adv. Energy Mater.*, 2011, **5**, 546–550.
31 T. Kasuga, M. Hiramatsu, A. Hoson, T. Sekino and K. Niihara, *Langmuir*, 1998, **14**, 3160–3163.
32 T. Kasuga, M. Hiramatsu, A. Hoson, T. Sekino and K. Niihara, *ChemInform*, 1999, **11**, 15.
33 J.-Y. Liao, B.-X. Lei, H.-Y. Chen, D.-B. Kuang and C.-Y. Su, *Energy Environ. Sci.*, 2012, **5**, 5750–5757.
34 T. Shibata, N. Sakai, K. Fukuda, Y. Ebina and T. Sasaki, *Phys. Chem. Chem. Phys.*, 2007, **9**, 2413–2420.
35 K. Okada, Y. Tokudome, P. Falcaro, Y. Takamatsu, A. Nakahira and M. Takahashi, *Chem. Commun.*, 2012, **48**, 6130–6132.
36 C. Wang, L. Yin, L. Zhang, Y. Qi, N. Lun and N. Liu, *Langmuir*, 2010, **26**, 12841–12848.
37 X. Xin, J. Wang, W. Han, M. Ye and Z. Lin, *Nanoscale*, 2012, **4**, 964–969.
38 M. D. Ye, X. K. Xin, C. J. Lin and Z. Q. Lin, *Nano Lett.*, 2011, **11**, 3214–3220.
39 J. Li, W. Wan, F. Zhu, Q. Li, H. Zhou, J. Li and D. Xu, *Chem. Commun.*, 2012, **48**, 389–391.
40 L. Zhang, Q. Ding and Y. Zhou, *Cryst. Res. Technol.*, 2011, **46**, 11.
41 M. Kruk and M. Jaroniec, *Chem. Mater.*, 2001, **13**, 3169–3183.
42 J. Jiang, F. Gu, W. Shao and C. Li, *Ind. Eng. Chem. Res.*, 2012, **51**, 2838–2845.
43 F. Fabregat-Santiago, G. Garcia-Belmonte, I. Mora-Sero and J. Bisquert, *Phys. Chem. Chem. Phys.*, 2011, **13**, 9083–9118.
44 X. Sun, Y. Liu, Q. Tai, B. Chen, T. Peng, N. Huang, S. Xu, T. Peng and X.-Z. Zhao, *J. Phys. Chem. C*, 2012, **116**, 11859–11866.
45 A. Hauch and A. Georg, *Electrochim. Acta*, 2001, **46**, 3457–3466.